# Plasma screening effects on proton-impact excitation of positive ions

K. Scheibner
*Joint Institute for Laboratory Astrophysics, University of Colorado and National Bureau of Standards, P.O. Box 440, Boulder, Colorado 80309-0440*
*and Physics Department, Lawrence Livermore National Laboratory, University of California, P.O. Box 808, Livermore, California 94550*

J. C. Weisheit
*Physics Department, Lawrence Livermore National Laboratory, University of California, P.O. Box 808, Livermore, California 94550*

N. F. Lane*
*Joint Institute for Laboratory Astrophysics, University of Colorado and National Bureau of Standards, P.O. Box 440, Boulder, Colorado 80309-0440*
(Received 3 March 1986)

We investigate the role of plasma screening in fine-structure excitation of excited ($n=2$) hydrogenic ions, $He^+$, $Ne^{9+}$, $Ar^{17+}$, and $Fe^{25+}$ in collisions with protons. Within the context of the semiclassical, impact-parameter formalism, both ion-sphere and Debye-Hückel static screening models have been used. For certain plasma conditions, the former model is easily justified by arguments based on the ordering of various time scales; however, the latter model is more appropriate for many plasmas presently subject to spectroscopic analysis. Substantial (e.g., factor-of-10) reductions from unscreened cross-section values are readily achievable. We discuss numerous qualitative trends exhibited by the screened cross sections, and obtain empirical relations that roughly scale the cross sections for different charges of the target ion.

## I. INTRODUCTION

Understanding the characteristics of hot plasmas requires a detailed knowledge of various processes, including excitation due to electron and ion collisions. Rate coefficients for these and other processes are required for interpretation of measured line intensities and for inferring important plasma parameters such as electron temperature and density.[1] Therefore, a large amount of effort has been devoted to calculating the corresponding cross sections to sufficient accuracy. A common feature of most calculations is that the plasma environment (within which these basic atomic processes take place) is usually ignored. The collision interactions which drive transitions, for example, are typically taken to be those relevant to an isolated system.[2]

It is well known, however, that the extreme conditions of some plasma environments can drastically alter transition rates from their values for the corresponding isolated systems. Long-range Coulomb interactions are screened by plasmas, leading to shorter-range interactions.[3] Some progress has been made in understanding the influence of the plasma on elastic ion-ion scattering,[4] atomic structure,[5] radiative processes,[6] and on inelastic electron collisions with atomic ions.[7–10] These later investigations were undertaken, in part, because of the dominant contribution made by electron impacts to ion-excitation rates when the plasma temperature $kT$ is much less than the threshold energy of the excitation $\Delta E$.[2,11,12] The effect of the plasma was modeled in these collision studies by static screened interactions, the justification of which requires some rather specific conditions.[13] First, the reciprocal of the electron-ion collision duration, $1/\tau_{ei}=\omega_{ei}$, must be less than the plasma (electron) frequency, $\omega_e=(4\pi e^2 N_e/m_e)^{1/2}$, where $N_e$ is the number density of plasma electrons. If this condition is not met, plasma screening of the target may not be accurately represented by a potential arising from the *average* electronic charge density in the ion's vicinity. Second, substantial screening of the electronic (i.e., scattering-electron—bound-electron) interaction is achieved only when $\Delta E<\hbar\omega_e$; otherwise the bound electron's motion also is too rapid to permit screening by most of the free electrons. (These statements follow from the fact that the plasma dielectric function is well approximated by unity for $\omega>\omega_e$, and by its static value for $\omega<\omega_e$.[14])

On the other hand, a static screening approach to plasma effects on ion-ion collisional cross sections is more easily justified. First, owing to the large mass of positive ions compared to the electron mass, the relative speed (and hence $1/\tau_{ii}=\omega_{ii}$) in an ion-ion collision is much smaller. Thus the inequality $\omega_{ii}\ll\omega_e$ is much less restrictive. Also, because the incident charge is screened—and effectively reduced—by plasma electrons, the interaction causing the transition is strongly reduced. Furthermore, in the absence of plasma screening, it is known that as the ratio of $kT/\Delta E$ increases, the relative importance of ion-impact excitation increases with respect to

 

electron-impact excitation.[2] These considerations have led to the present investigation of plasma effects on ion-impact excitation and deexcitation cross sections for transitions between the fine-structure levels of hydrogenlike ions, within the context of a static screening picture of the plasma.

The paper is organized as follows. In Sec. II the theoretical approach is outlined within the semiclassical, impact-parameter distorted-wave approximation; the influence of the plasma is represented by a static model potential. Various detailed results are developed in the appendixes. Specific formulas are given for the (structureless) ion-impact excitation of fine-structure levels of hydrogenlike ions. In Sec. III results are presented for the example of proton-impact excitation and deexcitation transitions between the ($n=2$) fine-structure levels of hydrogenlike argon. Both ion-sphere and Debye-Hückel models of the plasma screening are studied, and the influence of the plasma environment on the cross section is demonstrated and discussed for a variety of plasma conditions. In Sec. IV the dependence of the cross sections on nuclear charge and empirical scaling relations are considered. Comparisons are made for several different systems. The body of the paper concludes with a brief summary of the results.

## II. THEORETICAL APPROACH

### A. The semiclassical method

The specific processes examined in the present study are fine-structure transitions in hydrogenlike ions due to a collision with another (structureless) ion. Because of the large masses involved, the de Broglie wavelength is always much smaller than the classical distance of closest approach. To a good approximation the relative motion of the two nuclei can therefore be treated classically, and only the electron dynamics need be treated quantum mechanically; the problem is thus explored by means of the impact-parameter method.

The coordinate system chosen to characterize the ion-ion scattering process is shown in Fig. 1. A laboratory-fixed system has been chosen with $\hat{\mathbf{z}}$ defined by the initial relative momentum and with the origin taken to be the nucleus (with charge $Z_A$) of the hydrogenlike target ion. With respect to this origin, the bound electron is positioned at $\mathbf{r}$ and the projectile ion of net charge $Z$ is located at $\mathbf{R}$. The impact parameter vector $\boldsymbol{\rho}$ is perpendicular to the initial relative velocity $\mathbf{v}_0$. The dynamics of the atomic target are governed by the time-dependent Schrödinger equation, which yields the following coupled equations for the amplitudes of transition $b_{\beta\alpha}$ between an initial state $\alpha$ and final state $\beta$:

$$i\hbar\dot{b}_{\beta\alpha}=\sum_{\gamma\ (\neq\beta)} V_{\beta\gamma}e^{i\Delta_{\beta\gamma}(t)}b_{\gamma\alpha}\ . \tag{1}$$

(Throughout, $\alpha$, $\beta$, and $\gamma$ are used generically to indicate all the quantum numbers that uniquely specify the unperturbed target states.) The phase $\Delta_{\beta\gamma}(t)$ in Eq. (1) is defined by a first-order differential equation,

$$\hbar\dot{\Delta}_{\beta\gamma}=E^0_\beta-E^0_\gamma+V_{\beta\beta}(t)-V_{\gamma\gamma}(t)\ , \tag{2}$$

with the initial condition $\Delta_{\beta\alpha}(-\infty)=0$. $E^0_\beta$ and $E^0_\gamma$ are the energies of the unperturbed states $|\beta\rangle$ and $|\gamma\rangle$, respectively, and are obtained for the present study from the work of Erickson.[12] Note that by using unperturbed target states and their corresponding energies, we are ignoring the small plasma distortion, as evidenced by "plasma polarization shifts," of the target states $|\alpha\rangle$. (See Ref. 13 for a summary of several experimental results.) In addition, fine-structure transition energies $\Delta E$ usually are much less than the collision energies of primary interest, and at these energies the cross sections are insensitive to the small changes expected for $\Delta E$. The matrix element $V_{\beta\gamma}\equiv\langle\beta|V_e|\gamma\rangle$ between states $|\beta\rangle$ and $|\gamma\rangle$ involves the electronic part of the ion-ion interaction potential [cf. Eqs. (4) and (5) below]; spin-dependent interactions between projectile and target are neglected.

Once the amplitudes of Eq. (1) have been obtained, the cross section for the transition $\alpha\rightarrow\beta$ can be determined, in the impact-parameter method, from the relation

$$\sigma(\beta\leftarrow\alpha)=\int_0^{2\pi}d\phi'\int_0^\infty d\rho\,\rho\,|b_{\beta\alpha}(t\rightarrow\infty)|^2\ , \tag{3}$$

where $\phi'$ is the azimuthal scattering angle. The asymptotic probabilities depend on $\rho$ and $\theta'$ implicitly through their dependence on the electronic coupling.

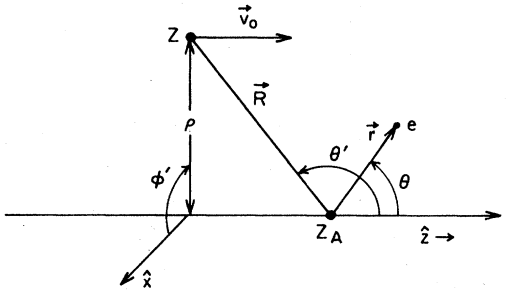


FIG. 1. Coordinate system for a collision of a structureless ion of net charge $Z$ with a hydrogenlike ion of nuclear charge $Z_A$. The $\hat{\mathbf{z}}$ axis is defined by the initial relative velocity $\mathbf{v}_0$. The bound-electron position is specified by $r$, $\theta$, and $\phi$ and the projectile by $R$, $\theta'$, and $\phi'$.

### B. Plasma models

The influence of the plasma on ion-impact excitation of the hydrogenic ions is approximated here by one of two static model potentials. In the limit of low temperatures and high densities, the mean electrostatic interaction energy is much greater in magnitude than the mean kinetic energy of the ions. A reasonable model of the plasma under these conditions is one in which each ion of charge $Z$ is surrounded by a sphere of radius $R_Z=(3Z/4\pi N_e)^{1/3}$ containing $Z$ uniformly distributed free electrons.[13] In this ion-sphere picture the interaction between a slow (speed $\ll\sqrt{kT/m_e}$) screened incident ion and a fast (speed $\gg\sqrt{kT/m_e}$) unscreened bound electron is approximately

$$V_e(\mathbf{R},\mathbf{r})=\begin{cases}-\dfrac{Z}{|\mathbf{R}-\mathbf{r}|}\left[1-\dfrac{R}{2R_Z}\left[3-\dfrac{R^2}{R_Z^2}\right]\right], & R\le R_Z\\ 0, \quad R>R_z \text{ (ion-sphere)} .\end{cases} \tag{4}$$

In the opposite limit of high temperatures and low densities, the mean thermal energy of the particles is much greater than the magnitude of their mean electrostatic interaction energy. Linearization of the Poisson-Boltzmann equation leads to the Debye-Hückel potential,[3]

$$V_e(\mathbf{R},\mathbf{r})=-\frac{Z}{|\mathbf{R}-\mathbf{r}|}e^{-R/D} \text{ (Debye-Hückel)} , \tag{5}$$

for the interaction of an unscreened bound electron and an ion screened only by plasma electrons, viz., $D=(kT/4\pi e^2N_e)^{1/2}$. (For simplicity, the screening effect in both the ion-sphere and the Debye-Hückel pictures is taken to be spherically symmetric, i.e., to depend only on $|\mathbf{R}|$ and not $|\mathbf{R}-\mathbf{r}|$. Because the time-averaged value of $\mathbf{r}$ is much less $R_Z$ or $D$ we can think of this simplification, which is justified when the bound electron's orbital motion is on a time scale $\ll 1/\omega_e$, as equivalent to performing a short time average.)

To calculate the transition amplitudes of Eqs. (1) and (2) in the semiclassical approximation, one must determine the time dependence of $\mathbf{R}$ by solving Newton's equation of motion. The ion-ion interaction potentials used to calculate the classical trajectory for the two static plasma models are derived and discussed in Appendix A. The results are given in Eqs. (6) and (7),

$$V_n(R)=\begin{cases}\dfrac{(Z_A-1)Z}{R}\left[1-\dfrac{R}{2R_n}\left[3-\dfrac{R^2}{R_n^2}\right]\right], & R\le R_n\\ 0, \quad R>R_n \text{ (ion-sphere)} ;\end{cases} \tag{6}$$

$$V_n(R)=\frac{(Z_A-1)Z}{R}\left[1-\frac{R}{2D}\right]e^{-R/D} \text{ (Debye-Hückel)} . \tag{7}$$

In Eq. (6), $R_n=[3(Z+Z_A-1)/4\pi N_e]^{1/3}$ is the ion-sphere radius in the united-ion limit, $R\to 0$. Note that, in both cases, the influence of the bound electron on the trajectory is approximated by using the net charge, $Z_A-1$ of the hydrogenic target.

In summary, the cross sections are calculated from Eq. (3) by numerically solving the coupled equations for the transition amplitudes for a projectile of net charge $Z$ [Eqs. (1) and (2)]. It should be emphasized that the *coupled* equations must be solved because in the present application the coupling between states is so strong that the transition amplitudes computed in first-order perturbation theory seriously violate unitarity. The electronic interaction potential [either Eq. (4) or (5)] depends not only on the electronic coordinates but also on the internuclear separation, which is determined by solving Newton's equation of motion using the nuclear-nuclear interaction potential of Eq. (6) or (7).

Several comments about these model potentials are appropriate. First, in contrast to the electron scattering problem, an unscreened bound electron interacts with a screened projectile ion (via $V_e$ above); also, the target *and* projectile are screened, leading to the ion-ion interaction $V_n$. Second, in order that the calculated cross sections are to be of any significance, the binary collision picture must be valid, that is, strong collisions must be well separated in time. If $R_\sigma\sim(\sigma/\pi)^{1/2}$ is taken to give a measure of the size of the strong-interaction region, the binary-collision approximation restricts the ionic number density $N_Z$ ($\sim N_e/Z$) according to $(4\pi/3)R_\sigma^3N_Z<1$. For the ion-sphere model, $R_\sigma<R_Z$ so that this restriction is always satisfied. However, the ion-sphere model represents only the strong-screening limit, and, in most plasma regimes now accessible in laboratory experiments, the Debye-Hückel model accurately represents static Coulomb screening at large internuclear separations, $R>R_Z$.[3,15] Under conditions such that the Debye-Hückel model is valid for all $R$, the binary collision restriction may not be satisfied. Thus, it seems worthwhile to determine the qualitative differences between the ion-ion inelastic cross sections computed with the short-range, ion-sphere interaction and those computed with the longer-range, Debye-Hückel interaction. Furthermore, cross sections for the Debye-shielded ions will be needed eventually to determine when the static screening and binary collision approximations actually do break down. When this occurs it will be necessary to replace the usual binary transition rates $N_Z\langle\sigma v_0\rangle$ by rates due to the fluctuating microfield of all the plasma ions (cf. Refs. 16 and 17). Finally, we point out that at very high, yet experimentally accessible densities the plasma frequency can exceed $\Delta E/\hbar$ for some fine-structure transitions; roughly this occurs when $N_e>10^{19}Z^4/n^3$ cm$^{-3}$. In such instances, the interaction $V_e$ is further reduced and the influence of plasma screening is even greater than that which we compute. We do not consider this effect here.

### C. The collision algebra

Calculation of the cross sections requires a fair amount of algebra which has been worked out in various forms by several authors (cf. Refs. 18 and 19). We include it for completeness and also because the required radial integrals are calculated more generally here than in other treatments.

The target fine-structure states are uniquely determined in an $\boldsymbol{l}\cdot\mathbf{S}$ coupling scheme by specifying the total angular momentum $\mathbf{J}$, the orbital angular momentum $\boldsymbol{l}$, the total spin $\mathbf{S}$, and $M_J$, the (laboratory fixed) $\hat{\mathbf{z}}$ projection of $\mathbf{J}$. These states are constructed in the usual way[20] from atomic basis states,

$$|l,S,J,M_J\rangle=(-1)^{S-l-M_J}\sum_{M_l=-l}^{l}\sum_{M_S=-S}^{S}(2J+1)^{1/2}\begin{pmatrix}l & S & J\\ M_l & M_S & -M_J\end{pmatrix}|lM_lSM_S\rangle . \tag{8}$$

(For hydrogenic target ions $S=\frac{1}{2}$, but for generality we carry $S$ in the notation and substitute the value $\frac{1}{2}$ only at the end.) Since these states depend only on the electronic coordinates, the matrix elements of Eqs. (1) and (2), for either of the electronic potentials [Eqs. (4) and (5)], are simply proportional to $\langle\beta|[1/(|\mathbf{R}-\mathbf{r}|)]|\gamma\rangle$ (here, $\beta=\{l,S,J,M_J\}$). This, of course, would not be true if the screening factors of Eqs. (4) and (5) also depended on $\mathbf{r}$; then, the matrix elements would be much more complicated and would differ in the two scaling models by more than a multiplicative term. Since no new basic features are expected to result from this additional complication, it is simply ignored, and the (screened) potentials of Eqs. (4) and (5) are used.

The matrix elements $W_{\beta\gamma}\equiv\langle\beta|[1/(|\mathbf{R}-\mathbf{r}|)]|\gamma\rangle$ are derived in detail in Appendix B, and the results are given below,

$$W_{\beta\gamma}=A(\beta,\gamma)\sum_{M_S=-S}^{S}(-1)^{M_l}\begin{pmatrix} l & S & J \\ M_l & M_S & -M_J\end{pmatrix}\begin{pmatrix} l' & S & J' \\ M_l' & M_S & -M_J'\end{pmatrix}$$
$$\times\sum_{\lambda=|l-l'|}^{l+l'}Y_{\lambda\mu}^{*}(\theta',\phi')\begin{pmatrix} l & \lambda & l' \\ 0 & 0 & 0\end{pmatrix}\begin{pmatrix} l & \lambda & l' \\ -M_l & \mu & M_l'\end{pmatrix}y_\lambda(nl,n'l')\ , \tag{9}$$

where $\lambda+l+l'$ is even, $M_l=M_J-M_S$, $M_l'=M_J'-M_S$, $\mu=M_J-M_J'$, and $\lambda\geq\mu$. The normalization constant $A(\beta,\gamma)$ is given by

$$A(\beta,\gamma)=(-1)^{2S-l-l'-M_J-M_J'}$$
$$\times[4\pi(2J+1)(2J'+1)(2l+1)(2l'+1)]^{1/2}\ . \tag{10}$$

Using the notation of Ref. 19, $y_\lambda(nl,n'l')$ in Eq. (9) is the radial integral

$$y_\lambda(nl,n'l')=\int_0^\infty r^2\frac{r_<^\lambda}{r_>^{\lambda+1}}\mathscr{R}_{nl}(r)\mathscr{R}_{n'l'}(r)dr\ , \tag{11}$$

where $r_<$ ($r_>$) is the smaller (larger) of $r$ and $R$, and $\mathscr{R}_{nl}$ is the radial portion of the hydrogenic wave function for a given $n$ and $l$. These radial integrals are worked out for any $n=n'$ and arbitrary $l$ and $l'$ in Appendix C. It is noted, however, that, following Seaton,[2] many authors have used the large-$R$ limiting form of these integrals,[21] which gives an incorrect high energy dependence of the cross sections. Since the exact form is only slightly more complicated it is used for the present calculations.

Finally, the spherical harmonic $Y_{\lambda\mu}$ of Eq. (9) depends on $\theta'$, the scattering angle with respect to the $+\hat{\mathbf{z}}$ axis (cf. Fig. 1) and the azimuthal scattering angle $\phi'$. Because the nuclear-nuclear interaction potentials of Eqs. (6) and (7) are both spherically symmetric, $\phi'$ remains constant in time; $\theta'$, on the other hand, is time dependent and is determined by solving Newton's equation of motion.

We now restrict attention to the $n=2$ manifold of fine-structure states and consider the scope of the cross-section calculations. The first simplification is to truncate the sum of Eq. (1) to include only the states of the relevant manifold. In this case there are eight states, which are denoted by $2\,^2S_{1/2,\pm1/2}$, $2\,^2P_{1/2,\pm1/2}$, $2\,^2P_{3/2,\pm3/2}$ and $2\,^2P_{3/2,\pm1/2}$, using the notation $n^{2S+1}L_{J,M_J}$. The truncation is justifiable because the splittings of the fine-structure levels are very small compared to the $\Delta n\neq0$ splitting. (The maximum fine-structure splitting for $Ar^{17+}$ is about 0.2 a.u., whereas the separation between the $n=2$ and 3 manifolds is about 20 a.u.) Thus for each initial state $|\alpha\rangle$, the restricted set of coupled equations [Eq. (1)], with the coupling given by Eqs. (4) or (5) and (9)–(11), involves these eight states. The system possesses a large degree of symmetry, however, which greatly simplifies the calculation, and is thus worth noting. The matrix elements exhibit two basic types of symmetry [easily verified by inspection of Eqs. (9)–(11)],

$$W_{\beta\gamma}=W_{\gamma\beta} \tag{12}$$

and

$$W(\beta=J,l,M_J;\gamma=J',l',M_J')$$
$$=(-1)^{l+l'+J+J'+M_J-M_J'+1}$$
$$\times W(\beta=J,l,-M_J;\gamma=J',l',-M_J')\ . \tag{13}$$

As a direct consequence of Eqs. (12) and (13), many of the matrix elements (64 possible for $n=2$) are either identical (to within a minus sign) or zero. For example, if $\beta=\{J,l,M_J\}$ and $\gamma=\{J,l,-M_J\}$ then $W_{\beta\gamma}=0$.

Further symmetry results from the law of reciprocity,[22] which states that

$$P(J,l,M_J\leftarrow J',l',M_J')=P(J,l,-M_J\leftarrow J',l',-M_J')\ , \tag{14}$$

where $P(\beta\leftarrow\alpha)=|b_{\beta\alpha}(t\rightarrow\infty)|^2$ is the probability of transition from $|\alpha\rangle$ to $|\beta\rangle$. Thus, the number of initial states which need to be considered is reduced from eight to four.

A final simplification occurs when one requires only cross sections $\sigma(lJ\leftarrow l'J')$, that are averaged over initial, and summed over final $M_J$ values. To see this consider such a cross section,

$$\sigma(J,l\leftarrow J',l')=\frac{1}{(2J'+1)}\int_0^{2\pi}d\phi'\int_0^\infty d\rho\,\rho\,\mathscr{P}_{J'l'}^{Jl}\ , \tag{15}$$

where

$$\mathscr{P}_{J'l'}^{Jl}=\sum_{M_J=-J}^{J}\sum_{M_J'=-J'}^{J'}P(J,l,M_J\leftarrow J',l',M_J')\ . \tag{16}$$

It is straightforward to show that (for $S=\frac{1}{2}$)

$$\mathscr{P}^{J,l}_{J',l'}=2\sum_{M_J=1/2}^{J}\sum_{M_J'=1/2}^{J'}[P(J,l,-M_J\leftarrow J',l',M_J')$$

$$+P(J,l,M_J\leftarrow J',l',M_J')] . \quad (17)$$

Therefore, to obtain all possible cross sections for transitions within the $n=2$ manifold, without regard to initial or final $M_J$, probabilities for only two initial states need to be calculated (e.g., $\alpha=\{J'=\frac{1}{2},\ l'=0,\ M_J'=\frac{1}{2}\}$ and $\alpha=\{J'=\frac{1}{2},\ l'=1,\ M_J'=\frac{1}{2}\}$). Note that Eq. (17) leads to the principle of detailed balance, which guarantees that

$$(2J'+1)(k')^2\sigma(J,l\leftarrow J',l')=(2J+1)k^2\sigma(J',l'\leftarrow J,l) . \quad (18)$$

(Here initial and final center-of-mass energies are taken to be identical.)

Though the above considerations lead to a greatly restricted number of initial states which need to be considered, there still are twenty-two coupled first-order equations which need to be integrated to obtain cross sections among the $n=2$ states. Sixteen pertain to the real and imaginary parts of the amplitudes of transition into the eight final states, two result from the second-order equation for $\ddot{R}$, and one from the first-order equation for the scattering angle $\dot{\theta}'$. The three remaining equations arise from Eq. (2), where the energies of the unperturbed target states depend only on $J$ and $l$ and the distortion terms $V_{\beta\beta}$ depend only on $J$, $l$, and $|M_J|$, as can be seen from inspection of Eq. (13): hence, there are only three unique (dynamic) splittings.

Calculation of the cross sections $\sigma(J,l\leftarrow J',l')$ requires the solution of the coupled equations over a range of impact parameters for a given model potential with the two initial conditions, $\alpha=\{\frac{1}{2},0,\frac{1}{2}\}$ and $\alpha=\{\frac{1}{2},1,\frac{1}{2}\}$. For a given (constant) azimuthal scattering angle $\phi'$ the target basis states contain the overall phase $e^{i\phi' M_J}$. Thus, no loss in generality results from the simple choice of $\phi'=0$. Because the transition probabilities have azimuthal symmetry, and only depend on the magnitude of the impact parameter, the cross section for a specific $(J,l,M_J\leftarrow J',l',M_J')$ transition is obtained from a single integration with respect to $\rho$. The $n=2$ manifold contains three unique cross sections (without regard to initial or final $M_J$), corresponding to the transitions $2\,^2S_{1/2}\leftrightarrow 2\,^2P_{1/2}$, $2\,^2S_{1/2}\leftrightarrow 2\,^2P_{3/2}$, and $2\,^2P_{1/2}\leftrightarrow 2\,^2P_{3/2}$. The calculations have been performed on a variety of host computers. On a VAX 8600 typically 70—120 CPU minutes were required to calculate the three Debye-Hückel cross sections for a given energy, screening length, and target ion. The analogous calculation of ion-sphere cross sections took about 30—40 CPU minutes. On a CRAY XMP the same calculations took about 6—8 CPU minutes and 3—4 CPU minutes, respectively.

## III. A SPECIFIC EXAMPLE: PROTON EXCITATION OF THE $n=2$ FINE-STRUCTURE OF HYDROGENLIKE ARGON

Figures 2, 3, and 5 summarize the results of the cross-section calculations for the specific example of $H^+ + Ar^{17+}(J',l')\rightarrow H^+ + Ar^{17+}(J,l)$ for a variety of plasma conditions, as represented by the parameters of the ion-sphere and Debye-Hückel model potentials. (Other examples are discussed in Sec. IV.) A detailed comparison of these cross sections is useful in understanding the effect of the plasma on these atomic processes.

TABLE I. Unperturbed fine-structure splittings $[E(2\,^2P_{1/2})=0]$ (from Ref. 12). Numbers in square brackets are powers of ten by which the values are to be multiplied.

| $Z_A$ | Final state | Energy ($cm^{-1}$) | Energy (a.u.) |
|---|---|---|---|
| 2 | $2\,^2S_{1/2}$ | 0.4685 | 2.134[−6] |
| | $2\,^2P_{3/2}$ | 5.857 | 2.669[−5] |
| 10 | $2\,^2S_{1/2}$ | 1.631[2] | 7.430[−4] |
| | $2\,^2P_{3/2}$ | 3.673[3] | 1.673[−2] |
| 18 | $2\,^2S_{1/2}$ | 1.301[3] | 5.928[−3] |
| | $2\,^2P_{3/2}$ | 3.884[4] | 0.1770 |
| 26 | $2\,^2S_{1/2}$ | 4.720[3] | 2.151[−2] |
| | $2\,^2P_{3/2}$ | 1.711[5] | 0.7795 |

Table I contains the unperturbed level splittings in atomic units for all systems considered here. Figure 2 compares the three unique cross sections relevant to the $n=2$ fine-structure levels in the ion-sphere model with $R_Z=10a_0$, corresponding to $R_n=26.2a_0$; here, and in what follows, $R_Z$ is the incident proton's screening radius. Table II contains the numerical data corresponding to Fig. 2 and is included to allow convenient numerical comparison. The overall features of this figure are typical of the fine-structure cross sections, independent of plasma effects; all three cross sections rapidly approach zero at low energy because the ion-ion repulsion prevents significant interaction. At high energies the cross sections approach zero ($\sigma\propto 1/E$) because the collision time is too short to allow efficient transfer of energy. Three other

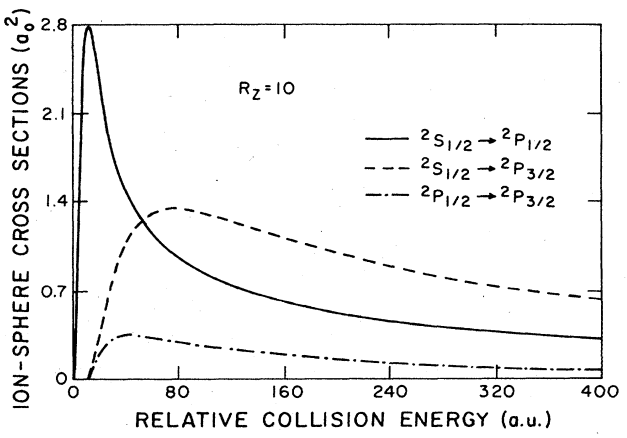


FIG. 2. Cross sections for the $n=2$ fine-structure transitions in hydrogenic argon due to proton collisions, for an ion-sphere plasma model of radius $R_Z=10a_0$. The quadrupole cross section is smaller than both dipole cross sections. The $\Delta J=0$ dipole cross section, which has the smallest excitation energy peaks at lower energies than the $\Delta J=1$ cross section.

TABLE II. Ion-sphere cross sections for $H^+ + Ar^{17+}$ collisions ($R_Z = 10a_0$). Numbers in square brackets are powers of ten by which the values are to be multiplied.

| Energy (a.u.) | Cross sections ($a_0^2$) $2\,^2S_{1/2} \rightarrow 2\,^2P_{1/2}$ | $2\,^2S_{1/2} \rightarrow 2\,^2P_{3/2}$ | $2\,^2P_{1/2} \rightarrow 2\,^2P_{3/2}$ |
|---|---|---|---|
| 1 | 7.566[−5] | 5.024[−09] | 6.671[−10] |
| 2 | 9.249[−2] | 1.503[−08] | 8.976[−09] |
| 4 | 0.9843 | 8.043[−08] | 1.715[−09] |
| 6 | 1.911 | 1.531[−05] | 3.532[−06] |
| 8 | 2.470 | 1.110[−03] | 3.527[−04] |
| 10 | 2.731 | 1.083[−02] | 4.296[−03] |
| 12 | 2.795 | 4.122[−02] | 1.926[−02] |
| 15 | 2.678 | 0.1316 | 7.050[−02] |
| 17 | 2.536 | 0.2132 | 0.1178 |
| 20 | 2.306 | 0.3506 | 0.1897 |
| 25 | 1.983 | 0.8645 | 0.2777 |
| 30 | 1.756 | 0.7960 | 0.3234 |
| 40 | 1.468 | 1.081 | 0.3544 |
| 60 | 1.150 | 1.324 | 0.3361 |
| 80 | 0.9674 | 1.351 | 0.2970 |
| 100 | 0.8424 | 1.311 | 0.2624 |
| 120 | 0.7507 | 1.248 | 0.2348 |
| 140 | 0.6792 | 1.180 | 0.2122 |
| 160 | 0.6215 | 1.115 | 0.1927 |
| 180 | 0.5736 | 1.053 | 0.1753 |
| 200 | 0.5331 | 0.9958 | 0.1597 |
| 250 | 0.4556 | 0.8765 | 0.1275 |
| 300 | 0.3982 | 0.7781 | 0.1038 |
| 400 | 0.3190 | 0.6328 | 7.313[−02] |
| 800 | 0.1783 | 0.3578 | 3.034[−02] |

features of these ion-ion excitation cross sections are worth noting. First, the peak of the $2\,^2S_{1/2} \rightarrow 2\,^2P_{1/2}$ cross section is greater than that for $2\,^2S_{1/2} \rightarrow 2\,^2P_{3/2}$, and occurs at a lower energy. This is because $\Delta E$ for the former transition is much smaller than that for the latter (0.0059 a.u. versus 0.18 a.u.). Second, at large energies where the cross sections are not as sensitive to the $\Delta E$ splitting, the ratio of the cross sections for the $\Delta J = 1$ to 0 dipole transitions becomes statistical, i.e., $(2\times\frac{3}{2}+1)/(2\times\frac{1}{2}+1)=2$. Finally, because the $1/R^3$ quadrupole coupling between $P$ states is of shorter range than the $1/R^2$ dipole coupling between $S$ and $P$ states, the quadrupole transition has the smallest cross section.

The above observations are characteristic of ion-impact excitations in general, and are not necessarily indicative of the plasma environment. Figures 3(a)—3(c), therefore, are included to compare individual cross sections for different screening lengths ($R_Z \propto N_e^{-1/3}$) as functions of the center-of-mass energy. The chosen plasma parameters were suggested by the work of Whitten, Lane, and Weisheit,[9] and are described in Table III. There are two major features of these results which we now discuss in turn. The first is how significantly the plasma can modify the collision process. In going from $R_Z = 10$ to 5 (corresponding to an increase in $N_e$ by a factor of eight) the cross section can change by as much as a factor of three. Indeed, the additional data points ($\times$) in these figures are the unscreened results of Walling and Weisheit,[23] each divided by a different constant factor to fit on the same scale. Thus, for all three transitions it is clear that plasma screening has a substantial effect. The second important feature in Fig. 3 concerns the relative positions of the cross-section maxima, $\tilde{E}_{\beta\alpha}(R_Z)$, considered as functions of screening length. For the $2\,^2S_{1/2} \rightarrow 2\,^2P_{1/2}$ transition it is observed that the maximum occurs at slightly lower energies as the screening length $R_Z$ is increased. For the other two transitions, the trend is reversed.

A qualitative, classical explanation of these trends can be obtained by assuming, for simplicity, that each transition occurs at some specific internuclear separation, say $R_t$. As the screening length $R_Z$ increases, so does the strength of the ion-ion repulsion and, consequently, this classical transition separation $R_t$ also increases; likewise, $R_t$ decreases when $R_Z$ decreases. Next we recall that the smaller the energy of transition, the lower the collision energy at which cross-section peak occurs. Therefore, if the "dynamical energy" splitting (i.e., the difference between fine-structure states including diagonal potential matrix elements),

$$\Delta E_{\beta\alpha}(R_t) = E_\beta^{(0)} - E_\alpha^{(0)} + W_{\beta\beta}(R_t) - W_{\alpha\alpha}(R_t) , \quad (19)$$

decreases with increasing $R_t$ (and, hence, increasing $R_Z$), the position $\tilde{E}_{\beta\alpha}$ of the peak also decreases; conversely, if $\Delta E_{\beta\alpha}(R_Z)$ increases with increasing $R_t$, $\tilde{E}_{\beta\alpha}$ will increase with increasing $R_Z$.

The dynamical energies of interaction (i.e., fine-structure energy plus diagonal potential matrix element)

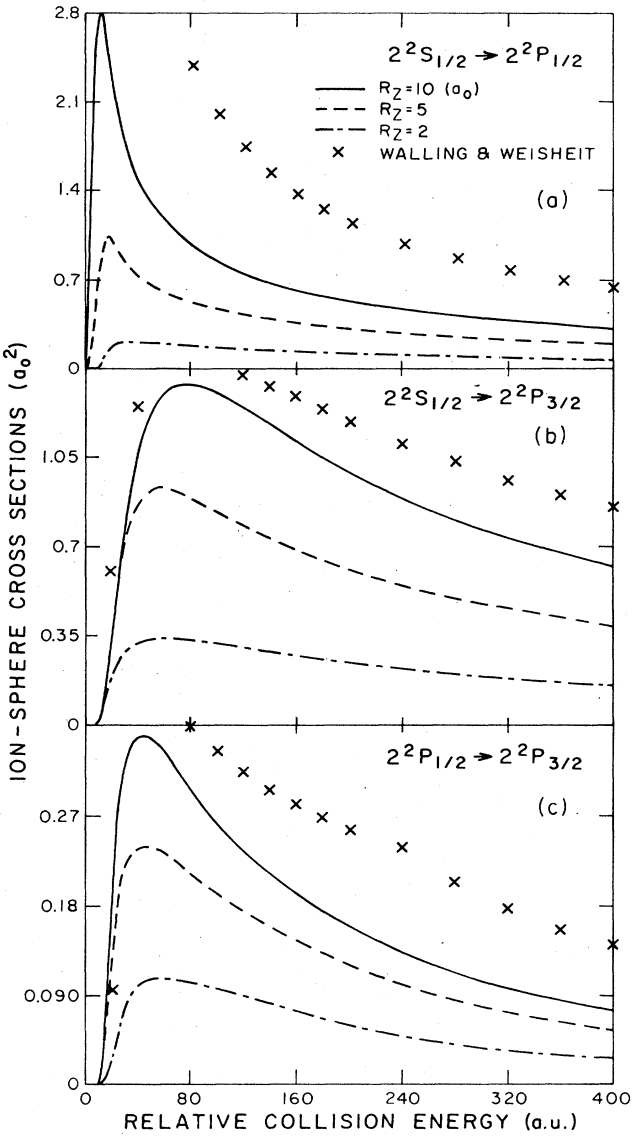


FIG. 3. Comparison of cross sections for different plasma parameters. Greater screening (smaller $R_Z$) yields smaller cross sections. The $\times$ data points are the unscreened results of Walling and Weisheit (Ref. 22), which have been divided by a factor of 5 in (a), by a factor of 3 in (b), and by unity in (c).

of Eq. (19) are plotted in Fig. 4 for the $H^+ + Ar^{17+}$ collision with $R_Z = 10a_0$. In the case of the $2\,^2S_{1/2} \rightarrow 2\,^2P_{1/2}$ transition, one can see in Fig. 4 (and inset) that as $R$ (and hence $R_t$) increases, the dynamic energy splitting between the distorted states decreases. Therefore, the cross-section maximum would be expected to occur at a relative energy that decreases with increasing $R_Z$. The opposite is true in the case of the $2\,^2S_{1/2} \rightarrow 2\,^2P_{3/2}$ transitions (assuming $R_t > 0.5a_0$); as $R_t$ increases, so do the energy splittings between these levels; thus the peaks in the corresponding cross sections occur at relative energies that increase with increasing $R_Z$. In the case of the quadrupole transition ($2\,^2P_{1/2} \rightarrow 2\,^2P_{3/2}$) some of the states move apart with increasing $R$ while others move together, so it is difficult to predict *a priori* the dependence on screening length of the energies at which these cross sections are maximal.

TABLE III. Plasma parameters. Numbers in square brackets are powers of ten by which the values are to be multiplied.

| Ion | $Z_A$ | $kT$ (eV) | Ne ($cm^{-3}$) | Screening length ($a_0$) |
|---|---|---|---|---|
| | | | Ion sphere | |
| $He^+$ | 2 | | 3.28[17] | $R_Z = 170$ |
| $Ne^{9+}$ | 10 | | 2.15[21] | 18.888 89 |
| $Ar^{17+}$ | 18 | | 2.74[22] | 10 |
| | | | 2.19[23] | 5 |
| | | | 3.42[24] | 2 |
| $Fe^{25+}$ | 26 | | 1.28[23] | 6.8 |
| | | | Debye-Hückel | |
| $Ne^{9+}$ | 10 | 500 | 2.77[22] | $D = 18.888\,89$ |
| $Ar^{17+}$ | 18 | 1000 | 1.97[23] | 10 |
| | | | 7.89[23] | 5 |
| $Fe^{25+}$ | 26 | 1500 | 6.40[23] | 6.8 |

This section concludes with a comparison of the cross sections for the two different plasma models. Figure 5 shows cross sections for each of the three fine-structure transitions calculated with the ion-sphere screening and $R_Z = 10a_0$, and with Debye-Hückel screening and $D = 10a_0$. For most energies considered here the trajectories resulting from the two nuclear potentials are very similar. The major difference in the cross sections therefore results from the difference in the electronic screening, which is greater for the ion-sphere potential than for the Debye-Hückel potential. Thus, as expected, for a given (equivalent) screening length, the cross sections are smaller in the former case than in the latter. The cross-section differences resulting from the two different potentials are less in the case of the quadrupole transition, owing to the

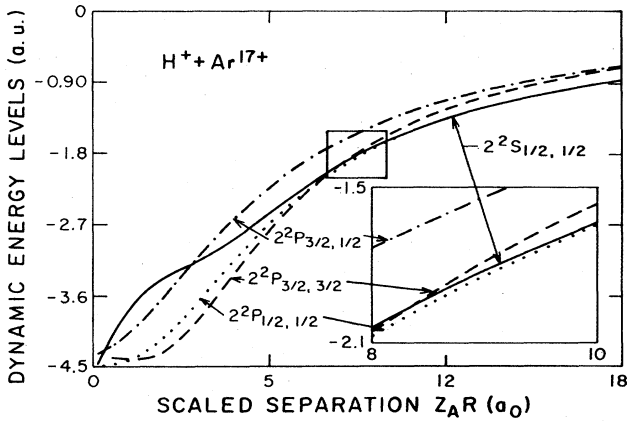


FIG. 4. Dynamic energy levels, as functions of internuclear separation. For separations greater than about $0.5a_0$, the dynamic $2\,^2S_{1/2}$ and $2\,^2P_{1/2}$ splitting decreases with increasing $R$, whereas the dynamic splitting between the $2\,^2S_{1/2}$ and $2\,^2P_{3/2}$ states increases with increasing $R$.

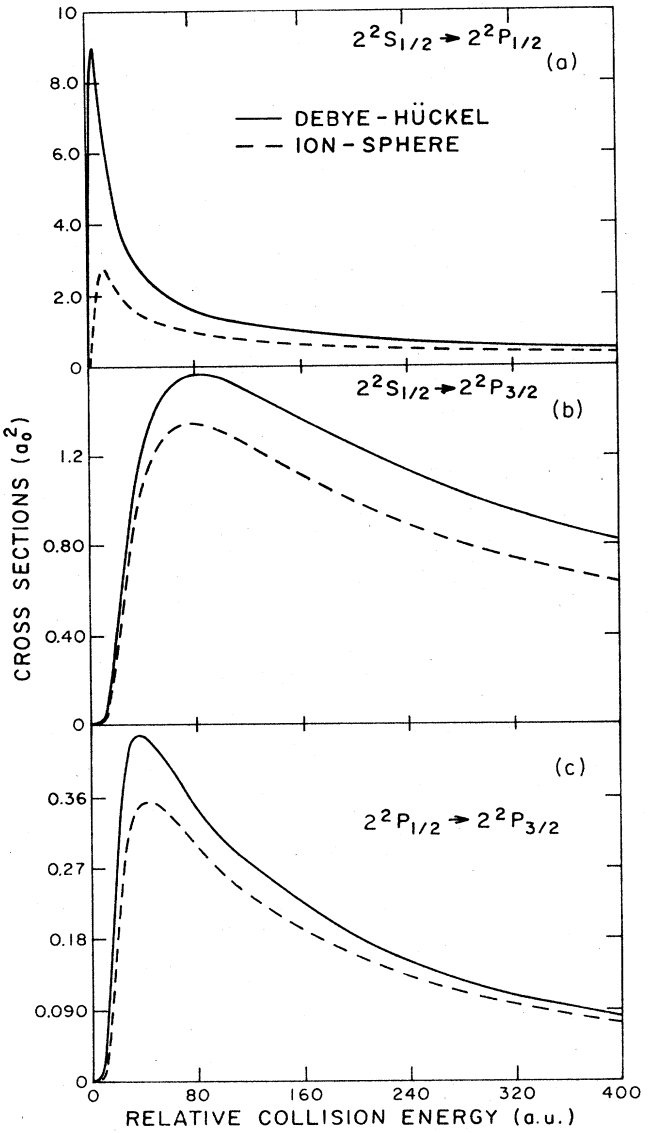


FIG. 5. Comparison of cross sections within the Debye-Hückel and ion-sphere plasma models. For this comparison, $D=R_Z$; the cutoff of the interaction is more severe in the ion-sphere model, leading to smaller cross sections. The quadrupole transition, being driven by an interaction that is shorter in range than those driving the dipole transitions, is less affected by the details of the plasma model.

inherently shorter range of the relevant electronic interaction.

An interesting trend is observed in the Debye-Hückel plasma model, and illustrated in Fig. 6; at medium to high energies, greater screening results in a lower $2^2S_{1/2} \rightarrow 2^2P_{3/2}$ cross section, whereas at lower energies the reverse is true. (This reversal is true for the other two transitions as well, except the switch occurs at lower energies.) To understand this behavior, it is useful to consider the classical turning point (at zero impact parameter, for simplicity) as a function of relative collision energy, for a range of Debye-Hückel screening lengths (see Fig. 7). At

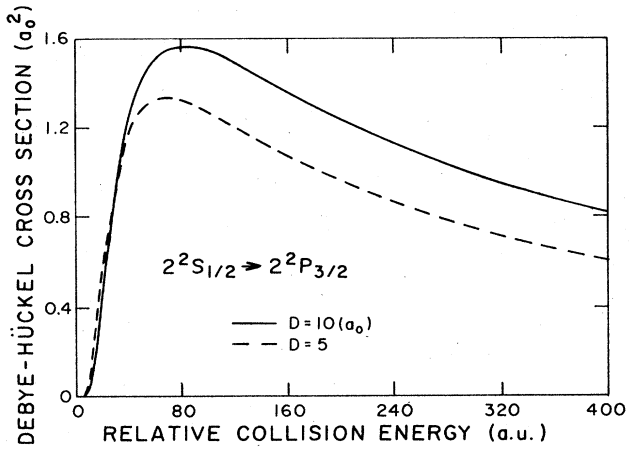


FIG. 6. Comparison of the cross sections for the $2^2S_{1/2} \rightarrow 2^2P_{3/2}$ transition for two difference screening lengths in a Debye-Hückel plasma. At low energies ($\lesssim 40$ a.u.) stronger screening permits a closer approach and a stronger collision. At higher energies, trajectories are nearly indistinguishable; the stronger the screening the smaller the cross section.

high energies, the classical turning point (i.e., where $\dot{R}=0$) is insensitive to variations in $D$; the only significant dependence of the cross section on $D$ arises through the cutoff factor $e^{-R/D}$. Thus, the cross section decreases with decreasing values of $D$. At low energies, on the other hand, the classical turning point is a strong function of $D$ (decreasing with decreasing $D$), and the ions can approach more closely when the screening is stronger (i.e., when $D$ is smaller). At sufficiently small energies the effect of reducing the Coulomb interaction is more than compensated for by the effect of allowing a closer approach. Thus, at lower energies, the cross section increases with decreasing values of $D$.

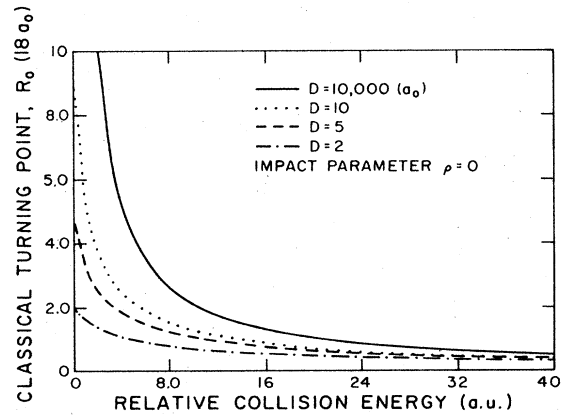


FIG. 7. Classical turning point as a function of relative collision energy (with $\rho=0$), for several Debye-Hückel screening lengths $D(a_0)$. At higher energies ($\gtrsim 40$ a.u.) the trajectory is not particularly sensitive to the screening. At low energies there is a significant trajectory effect, which can ultimately lead to an increase in cross section with increasing screening, as seen in Fig. 6.

The reason this trend is not observed for an ion-sphere interaction is slightly obscure, and perhaps artificial. For a given internuclear separation in the Debye-Hückel case, the nuclear-nuclear repulsion is of the same order of magnitude as the electronic interaction, because both interactions are reduced essentially by the factor $e^{-R/D}$. For our ion-sphere model, however, the electronic potential is cut off at $R=R_Z$, whereas the nuclear potential is cut off at $R=R_n=[(Z+Z_A-1)/Z]^{1/3}R_Z$, which can be significantly greater than $R_Z$. (In the case of $H^+ + Ar^{17+}$, $R_n=2.62R_Z$.) As a result, there exists a minimum energy, below which the ion-sphere radius $R_Z$ of the incident ion does not overlap with the bound electron, even though the two ions experience a repulsion. This minimum energy is given by the relation

$$E_{\min}=\frac{Z(Z_A-1)}{R_Z}\left\{1-\frac{1}{2}\left[\frac{Z}{Z+Z_A-1}\right]^{1/3}\times\left[3-\left[\frac{Z}{Z+Z_A-1}\right]^{2/3}\right]\right\}, \tag{20}$$

which increases with decreasing $R_Z$. Its value is 0.774 a.u. for the $H^+ + Ar^{17+}$ system with $R_Z=10a_0$. The trajectory effect, which in the Debye-Hückel model, at small energies, ultimately leads to greater cross sections with greater screening, is therefore missing in the ion-sphere model. To confirm that this explanation is correct, we calculated cross sections for the ion-sphere model potential with $R_n$ set arbitrarily equal to $R_Z$. The cross sections behave qualitatively like the Debye-Hückel cross sections at all energies. [In fact, when $R_Z \sim D/2$, the $S \rightarrow P$ cross sections are nearly equal (cf. Ref. 9).]

## IV. CROSS-SECTION DEPENDENCE ON TARGET NUCLEAR CHARGE

In Sec. III we discussed, in detail, proton-impact cross sections for transitions between the $n=2$ fine-structure levels of hydrogenlike argon. In this section we present the cross sections for the analogous transitions in $He^+$, $Ne^{9+}$, and $Fe^{25+}$ ions. We then explore possible scaling relations with respect to the target's nuclear charge $Z_A$. Our conclusion is that while there is no obvious analytical scaling for either plasma-model potential, comparisons of numerical results for several target systems suggest reasonable empirical scaling relations that may be useful in applications.

Figures 8(a)–8(c) illustrate the ion-sphere, proton-impact cross sections for hydrogenlike helium, neon, and iron targets. For each target ion the plasma density has been adjusted so that $R_Z \propto (Z_A-1)^{-1}$, with $R_Z(Ar^{17+})=10a_0$. This choice is made because the electronic potential depends on $1/|\mathbf{R}-\mathbf{r}|$ and the ratio $R/R_Z$. Thus for any convenient scaling relation it is important that $R$ and $R_Z$ have the same $Z_A$ dependence as $r \sim n^2 a_0/Z_A$. [Note that the ion-sphere radii are scaled by $(Z_A-1)$ rather than $Z_A$ because the nuclear potential, and hence the trajectories, depend on $(Z_A-1)$; except for helium, there is little difference between the two.] The neon and iron cross sections are similar to those of argon

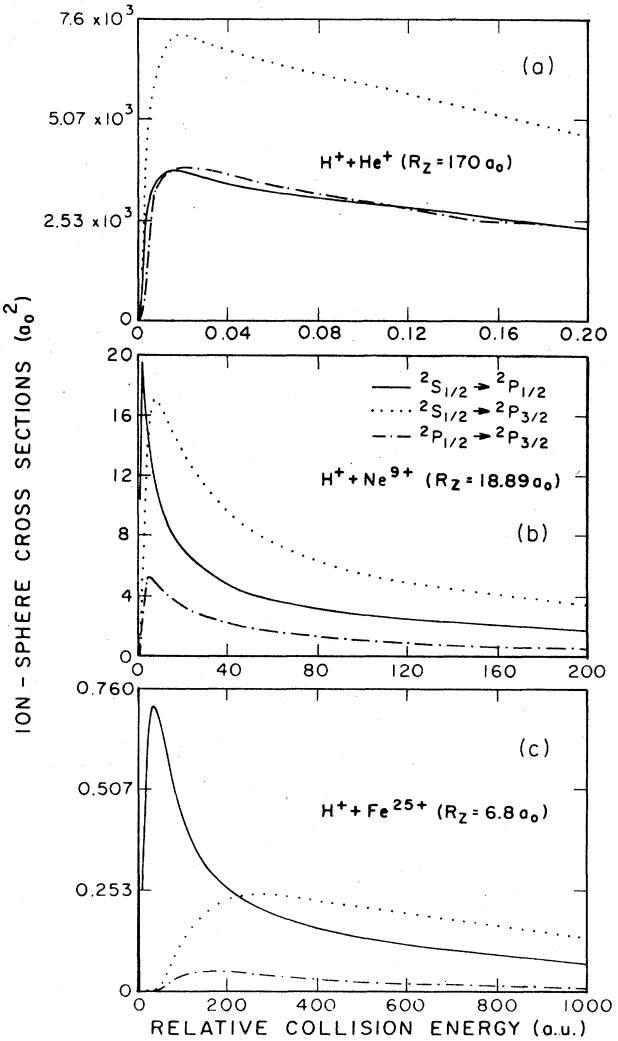


FIG. 8. The ion-sphere cross sections for the $H^+ + He^+$, $H^+ + Ne^{9+}$, and $H^+ + Fe^{25+}$ systems. For the $He^+$ target, at the energy where the $2\,^2S_{1/2} \rightarrow 2\,^2P_{1/2}$ transition would exhibit a strong peak in the unscreened cross section, the cross section is clearly suppressed. The nuclear repulsion prevents the bound electron from penetrating very deeply into the proton's ion sphere.

(cf. Fig. 2), whereas the helium results—especially for the $2\,^2S_{1/2} \rightarrow 2\,^2P_{1/2}$ transition—are very different. The qualitative difference of the helium system is understood as follows. As was mentioned in Sec. III the cross-section maximum occurs at a center-of-mass energy $\tilde{E}_{\beta\alpha}$ that is roughly proportional to the energy splittings between the levels; in the present case the relevant splittings are the fine-structure level separations, which scale roughly as $Z_A^4$. The minimum energy required for any significant contribution to the cross section, however, scales approximately as $E_{\min} \propto Z_A^2$ [cf. Eq. (20)]. For the $Ar^{17+}$ system, $E_{\min} \ll \tilde{E}_{\beta\alpha}$. But, as $Z_A$ decreases the energy at which the maximum occurs can become comparable to $E_{\min}$. When this happens, the peak value of the screened cross section will be greatly reduced. Since the $2\,^2S_{1/2} \rightarrow 2\,^2P_{1/2}$

splitting is the smallest of the levels considered here, the energy at which the corresponding cross-section maximum occurs is also smallest; therefore, the $2\,^2S_{1/2}\rightarrow 2\,^2P_{1/2}$ cross section will be affected the most. In the case of $He^+$, the cross section is so much reduced that at all energies it becomes comparable to that of the quadrupole transition. Since all three cross sections fall off as $1/E$ beyond their respective peaks, the reduced value of the peak cross section for the $\Delta J=0$ dipole transition, relative to the others, yields the observed trend.

The neon and iron systems, on the other hand, yield cross sections qualitatively similar to the argon results because in all three cases $E_{\min}$ is much less than the peak energies. This similarity suggests that the cross sections may exhibit an approximate $Z_A$ scaling.

At first glance, scaling in the ion-sphere collision problem seems untractable because the relevant lengths do not scale similarly. The electronic potentials [Eq. (4)] depend on $R$, $r$, and $R_Z$. Of course, $r$ varies as $Z_A^{-1}$. However, $R_Z$ depends on $Z$, not $Z_A$, and varies as $Z^{1/3}$. For comparison purposes, though, the plasma density can be adjusted (as we have done for Fig. 8) so that $(Z_A-1)R_Z=\text{const}$. The nuclear potential, however, depends on $R$ (which scales as $Z_A^{-1}$ [in the electronic problem and $(Z_A-1)^{-1}$ in Newton's equation]) and on the ratio $R/R_n$. Since $R_n=[(Z+Z_{A-1})/Z]^{1/3}R_Z$, which with the above scaling for $R_Z$ scales as $[(Z+Z_{A-1})Z]^{1/3}Z_A^{-1}$, the scaling of $V_n$ is unlike that of $V_e$. Thus, we might initially expect cross sections for different targets to be qualitatively different. This is, in fact, what we have already seen in the case of the $He^+$ target *vis-à-vis* the $Ar^{17+}$ target. The similarity of the neon and iron cross sections, however, reflects the fact that, for most energies under consideration, the trajectories are not strongly affected by the nuclear repulsion, and so there is only one important screening length, viz., $R_Z$. It is for this reason that the ion-sphere and Debye-Hückel results look so similar; there is only essentially one screening length important to either problem, $R_Z$ or $D$, respectively. In both plasma models, therefore, all lengths scale approximately as $Z_A^{-1}$, and thus it was hoped that the cross sections in both models might also scale simply. Unfortunately, the first-order differential equations do not lend themselves to any obvious scaling. To demonstrate this point, it is useful to consider the amplitudes of transition resulting from Eq. (1) in the limit when first-order perturbation theory is valid. In this case Eq. (1) becomes

$$i\hbar\dot{b}_{\beta\alpha}=V_{\beta\alpha}e^{i\Delta_{\beta\alpha}} . \tag{21}$$

Ignoring the distortion terms, the phase in Eq. (2) has a particularly simple form, and Eq. (21) becomes

$$i\hbar\dot{b}_{\beta\alpha}=V_{\beta\alpha}e^{i\omega_{\beta\alpha}t} , \tag{22}$$

where $\omega_{\beta\alpha}\equiv\dot{\Delta}_{\beta\alpha}=(E_\beta^0-E_\alpha^0)/\hbar$. By changing variables to $\tau=\omega_{\beta\alpha}t$, the probability amplitude becomes just

$$b_{\beta\alpha}=\frac{-i}{\hbar\omega_{\beta\alpha}}\int_{-\infty}^{\infty}V_{\beta\alpha}e^{i\tau}d\tau . \tag{23}$$

For a rectilinear trajectory, the internuclear coordinate is given by

$$R=[(v_0t)^2+\rho^2]^2=\left[\left[\frac{v_0\tau}{\omega_{\beta\alpha}}\right]^2+\rho^2\right]^{1/2} . \tag{24}$$

Since $V_{\beta\alpha}\propto\langle\beta|(1/|\mathbf{R}-\mathbf{r}|)|\alpha\rangle$, the ratio $V_{\beta\alpha}/Z_A$ is nearly independent of $Z_A$ provided $Z_AR_Z$, $Z_A\rho$, and $Z_Av_0/\omega_{\beta\alpha}$ are independent of $Z_A$. Thus, if the distortion terms are negligible, we have the scaling $Z_AR=\text{const}$, $(Z_A/\omega_{\beta\alpha})^2E=\text{const}$, and [cf. Eq. (3)] $\omega_{\beta\alpha}^2\sigma=\text{const}$. Now, for $\Delta n\neq 0$ transitions, $\omega_{\beta\alpha}\propto Z_A^2$ and the familiar[19] scaling ($Z_A^4\sigma=\text{const}$) results. In the present case, however, $\omega_{\beta\alpha}\propto Z_A^4$ and we have, instead, $E/Z_A^6=\text{const}$ and $Z_A^8\sigma=\text{const}$. We have found, however, that these scalings are not borne out in the calculations. For an $Ar^{17+}$ target the peak energy $\tilde{E}_{\beta\alpha}$ of the $2\,^2S_{1/2}\rightarrow 2\,^2P_{3/2}$ cross section [cf. Fig. 5(b)] occurs at a relative collision energy of $\sim 80$ a.u. The above scaling predicts that the peak of the cross section for a $Ne^{9+}$ target should occur at a relative energy of $\sim 80(\frac{10}{18})^6\sim 2.4$ a.u. The calculated $H^+ + Ne^{9+}$ results are shown in Fig. 8(b) where the peak is seen to occur instead of $\sim 10$ a.u. Moreover, for energies as large as 400 a.u., the cross sections for the $H^+ + Ar^{17+}$ system are all nearly proportional to $1/E$. The corresponding energy predicted in the $H^+ + Ne^{9+}$ system is $400(\frac{10}{18})^6\sim 12$ a.u., which is too small; for the $H^+ + Fe^{25+}$ system [Fig. 8(c)] the corresponding energy is predicted to be $400(\frac{26}{18})^6\sim 3600$ a.u., which is too large. The reason for the discrepancy is that the assumed $Z_A$ dependence of the phase in the above analysis is too strong; the distortion terms cannot be ignored. On the other hand, if the fine-structure splittings are completely neglected and only the distortion terms are retained, a similar analysis yields the approximate scaling $Z_AR=\text{const}$, $E=\text{const}$, $\omega_{\beta\alpha}/Z_A=\text{const}$, and $Z_A^2\sigma=\text{const}$. This behavior also is not borne out in the calculations, in this case, because the $Z_A$ dependence of the phase is too weak. The actual $Z_A$ dependence of the phase varies in time and is not simply proportional to a particular power of $Z_A$, but evidently stays between the linear and quartic relations.

In an attempt to extract an optimum empirical scaling, we begin by restating that the cross sections all fall off as $1/E$ for large energies. First, we choose to explicitly include the $Z_A$ dependence, and we have

$$\sigma(Z_A)E(Z_A)=B(Z_A)=B_0/Z_A^q , \tag{25}$$

where $B_0$ is some constant, and $q$ is a power to be determined. By comparing calculated values of $B(Z_A)$ for the three values of $Z_A$, we find that $q=2\pm 0.05$, where the uncertainty arises because $B(Z_A)$ is only approximately independent of $E(Z_A)$ at large, yet finite energies. Though obviously not a proof, this result suggests that the general scaling determined from perturbation theory is applicable at high energies, namely, $Z_AR=\text{const}$, $(Z_A/\omega_{\beta\alpha})^2E=\text{const}$ and $\omega_{\beta\alpha}^2\sigma=\text{const}$. To completely specify an empirical scaling we next attempted to determine the "effective" $Z_A$ dependence of $\omega_{ba}$ by assuming the form

$$\omega_{\beta\alpha}/Z_A^p=\text{const} . \tag{26}$$

To find the "best" value, we varied $p$ until—for the dif-

TABLE IV. Cross-section scaling parameters $p$, obtained from minimization using different energy moments $\mu_m$.

| $2\,^2S_{1/2}\rightarrow 2\,^2P_{1/2}$ | | | $2\,^2S_{1/2}\rightarrow 2\,^2P_{3/2}$ | | | $2\,^2P_{1/2}\rightarrow 2\,^2P_{3/2}$ | | |
|---|---|---|---|---|---|---|---|---|
| $m$ | $p$ | (Target ions used in fit) | $m$ | $p$ | (Target ions used in fit) | $m$ | $p$ | (Target ions used in fit) |
| 1 | 1.764 | ($Ar^{17+}$,$Fe^{25+}$) | 1 | 2.158 | ($Ar^{17+}$,$Fe^{25+}$) | 1 | 1.942 | ($Ar^{17+}$,$Fe^{25+}$) |
| 2 | 1.878 | | 2 | 2.146 | | 2 | 2.020 | |
| 4 | 1.924 | | 4 | 1.978 | | 4 | 2.120 | |
| 6 | 1.932 | | 6 | 1.964 | | 6 | 2.032 | |
| 8 | 1.934 | | 8 | 1.960 | | 8 | 2.006 | |
| 1 | 1.779 | ($Ne^{9+}$,$Ar^{17+}$,$Fe^{25+}$) | 1 | 2.105 | ($Ne^{9+}$,$Ar^{17+}$,$Fe^{25+}$) | 1 | 4.1785 | ($Ne^{9+}$,$Ar^{17+}$,$Fe^{25+}$) |
| 2 | 1.758 | | 2 | 2.059 | | 2 | 4.501 | |
| 4 | 1.709 | | 4 | 2.062 | | 4 | no minimum found | |
| 6 | 1.684 | | 6 | 2.082 | | 6 | for these moments | |
| 8 | 1.669 | | 8 | 2.096 | | 8 | | |

ferent choices of $Z_A$—the scaled cross sections as functions of the scaled energies were, in some way, closest. The method used was to minimize

$$\delta=[\mu_m(\max)-\mu_m(\min)]/[\mu_m(\max)+\mu_m(\min)] \quad (27)$$

with respect to $p$, where $\mu_m$ is the $m$th energy moment of the cross section,

$$\mu_m(Z_A)=Z_A^{-2[m(p-1)-1]}\int_0^{E_f(Z_A)}\sigma(Z_A)E^m(Z_A)dE(Z_A)\,. \quad (28)$$

The designation max (min) means the specific value of $Z_A$ which yields the largest (smallest) value of the $m$th moment. In Table IV we give the results of the minimization procedure for all three transitions and for various moments $m$.

Figure 9 shows the scaled cross sections versus the scaled energies for specific choices of $p$, for the particular case of a Debye-Hückel plasma. Similar scaling results from an ion-sphere plasma, but in either case the scaling is clearly only approximate. It is the absence of a simple scaling of $\Delta_{\beta\alpha}$ [cf. Eq. (2)], plus the additional complica-

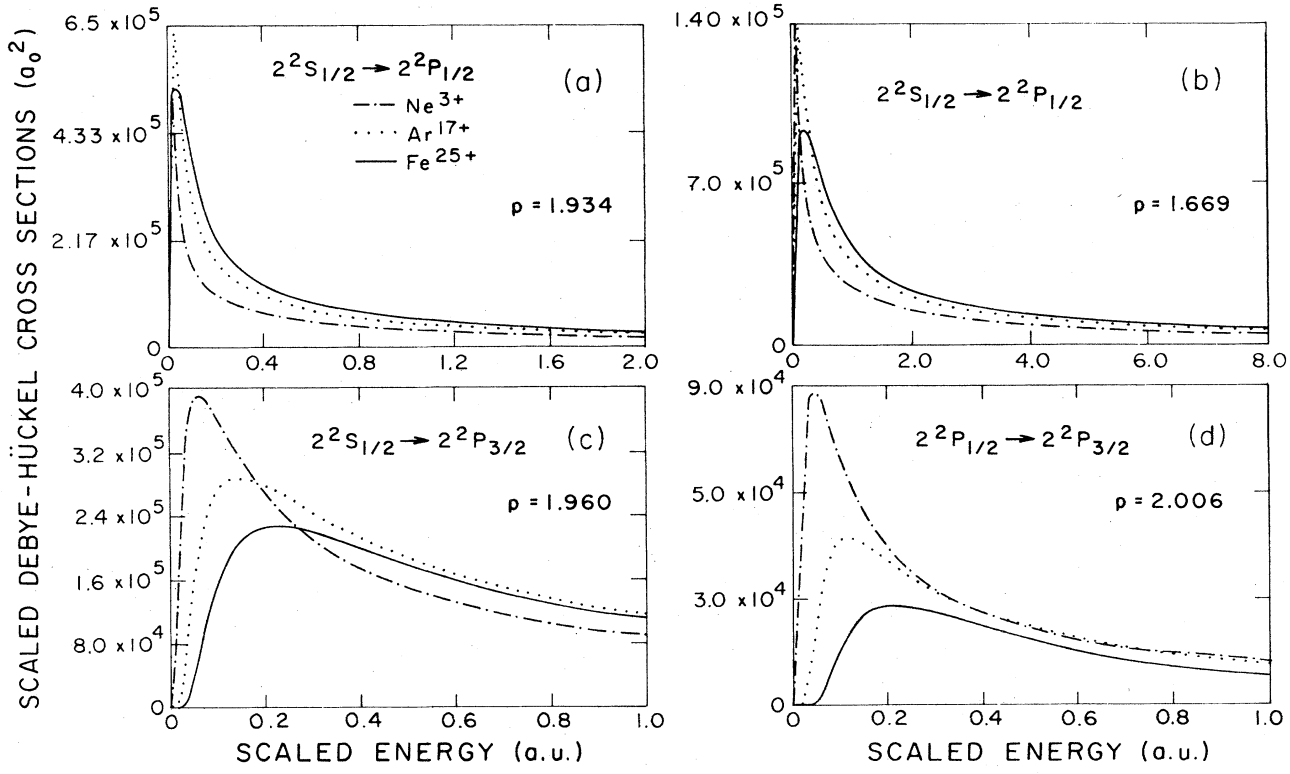


FIG. 9. Scaled Debye-Hückel cross sections vs scaled energy. The product of $\sigma(Z)E(Z)$ scales as $1/Z^2$. (The ion-sphere cross sections scale similarly.) Though these scalings are only approximate, a wide range of systems can be represented.

tion of all states being coupled, each with a different, time-dependent phase, that prevents the cross sections from exhibiting a precise scaling with respect to $Z_A$.

## V. SUMMARY

The present work represents, to our knowledge, the first study of dense-plasma effects on ion-impact excitation cross sections. The plasma environment has been included within the framework of two static screening models. The static approximation is valid as long as the plasma frequency $\omega_e$ is much greater than the reciprocal of the collision duration. We have examined fine-structure transitions, which correspond to small $\Delta E$, and have found the effects of the plasma environment, as characterized by plasma screening lengths representative of dense, high-temperature fusion plasmas, to be very large. The cross sections are sensitive to the screening length, the $\Delta E$ of the transition, and the collision energy. At most collision energies, the net effect of plasma screening is an overall reduction of the cross sections, the stronger screening causing the greater reduction. Quadrupole transitions, which result from a shorter-ranged interaction than the dipole interaction are not as sensitive to these screening effects. This conclusion is further supported by comparison of the cross sections calculated within the two plasma models; the quadrupole results are quite similar, whereas the dipole results are significantly different.

Finally, it has been demonstrated that, even though there is no obvious analytical scaling apparent in the coupled equations, approximate empirical scaling relations do exist which can be used to represent a wide range of systems and plasma environments.

## ACKNOWLEDGMENTS

One of the authors (K.F.S.) would like to express appreciation to the Lawrence Livermore National Laboratory (LLNL) for generous use of the laboratory facilities. Both K.F.S. and N.F.L. acknowledge the Joint Institute for Laboratory Astrophysics, where much of the research was performed. N.F.L. acknowledges the University of Colorado at Colorado Springs, where he was in residence while much of this research was performed. K.F.S. and N.F.L. are supported by U.S. Department of Energy (Office of Basic Energy Sciences) research contract to Rice University. J.C.W.'s work was performed under the auspices of the U.S. Department of Energy, and supported by Contract No. W-7405-Eng-48 to LLNL.

## APPENDIX A: THE ELECTROSTATIC INTERACTION OF SCREENED IONS

The mean potential energy of two ions and their attendant clouds of screening electrons is the interaction that regulates the ion-ion collision trajectory. This energy, $V_n(R)=-kT\ln[g_n(R)]$, is related to the ion-ion pair distribution $g_n(R)$, which measures the departure of the ionic density from its mean value. (See Ref. 24 for a thorough discussion of these concepts.) In this section we obtain simple, approximate expressions for $V_n(R)$ for two limiting cases: (1) the ion-sphere model, for plasmas in which Coulomb interactions strongly affect ion distributions; (2) the Debye-Hückel model, for plasmas in which Coulomb interactions only weakly affect ion distributions.

*Ion-sphere model.* The electrostatic self-energy of electrons in an ion sphere of radius $R_1$ surrounding a nucleus $Z_1$ is

$$V_{ee}^{(1)}=+\frac{3}{5}\frac{Z_1^2e^2}{R_1}\ , \tag{A1}$$

and the electrostatic energy of interaction between these electrons and the nucleus is

$$V_{ez}^{(1)}=-\frac{3}{2}\frac{Z_1^2e^2}{R_1}\ , \tag{A2}$$

where $\frac{4}{3}\pi R_1^3N_e=Z_1$. Thus, the total electrostatic energy due to plasma screening is

$$V^{(1)}=V_{ee}^{(1)}+V_{ez}^{(1)}=-\frac{9}{10}\frac{Z_1^2e^2}{R_1}\ . \tag{A3}$$

Consider first two nuclei, $Z_1$ and $Z_2$, with separation $R=0$. The total electrostatic energy due to screening in this case is simply

$$V^{(12)}=-\frac{9}{10}\frac{(Z_1+Z_2)^2e^2}{R_n}\ , \tag{A4}$$

where $\frac{4}{3}\pi R_n^3N_e=Z_1+Z_2$. Therefore, the net energy of interaction due to plasma screening is[24,25]

$$\begin{aligned}V(R=0)&=V^{(12)}-V^{(1)}-V^{(2)}\\&=-\frac{9}{10}e^2\left[\frac{4\pi N_e}{3}\right]^{1/3}\\&\quad\times[(Z_1+Z_2)^{5/3}-Z_1^{5/3}-Z_2^{5/3}]\ .\end{aligned} \tag{A5}$$

Next, let $Z_1$ be displaced a small distance $r_1\ll R_n$ from the center of this united-nucleus sphere, and let $Z_2$ be displaced a small distance $r_2$ in the opposite direction, so that $R=r_1+r_2$ is the internuclear separation. We assume that, as long as the two nuclei are close, the screening electrons form a spherical cloud whose center is positioned such that $V(R)$ is minimized. This gives the result

$$V(R\ll R_n)=V(0)+\frac{Z_1Z_2e^2}{2R_n}\left[\frac{R}{R_n}\right]^2\ . \tag{A6}$$

Addition of the Coulomb-repulsion term yields the total interaction energy of two nearly concentric ion spheres,

$$V_n(R\ll R_n)=\frac{Z_1Z_2e^2}{R}\left[1+\frac{1}{2}\left[\frac{R}{R_n}\right]^3-\frac{3}{2}\left[\frac{R}{R_n}\right]\left[\frac{3}{5}\frac{(Z_1+Z_2)^2-(Z_1+Z_2)^{1/3}(Z_1^{5/3}+Z_2^{5/3})}{Z_1Z_2}\right]\right]\ . \tag{A7}$$

Note that, except for the departure from unity of the rightmost term within large parentheses, this is just the interaction of one bare nucleus with an ion sphere of radius $R_n$ centered on the other nucleus; in fact, when $Z_1/Z_2$ is much larger or smaller than 1, the above factor in the rightmost large parentheses approaches 1.

Lastly, consider two ion spheres that barely overlap, viz., $\epsilon=1-R/(R_1+R_2)\ll 1$. In a first approximation, each screening cloud retains its own identity; thus the energy of interaction is just the overlapping volume integral of the (positive) potential of one ion sphere times the (negative) charge density of the other, and is therefore negative. This attraction, which is akin to the van der Waals interaction between two neutral atoms, is calculated to be very weak ($\sim\epsilon^4$),

$$V_n(R\lesssim R_1+R_2)=-\frac{Z_1Z_2e^2}{(R_1+R_2)}\left[\frac{3(R_1+R_2-R)^4}{16R_1^2R_2^2}\right]. \tag{A8}$$

When $R$ is neither very small nor very large ($\sim R_1+R_2$), we expect the composite screening cloud to be peanut shaped, as one characteristically has for a diatomic molecule. However, instead of solving a complicated—and somewhat artificial—electrostatics problem for the "true" interaction at arbitrary internuclear distances, we prefer to use some simple interpolation between the small- and large-$R$ formulas, Eqs. (A7) and (A8). After several expressions were tried, we settled on the formula given as Eq. (6) of the main text. It is nearly correct at small $R$ values, regardless of the value of $Z_1/Z_2$, and, although it fails to provide for any weak attraction at large $R$ values, its truncation at $R=R_n<R_1+R_2$ prevents too early an onset of the Coulomb repulsion between the two nuclei. Such a sharp cutoff in $V_n(R)$ does indeed occur in the high-density and low-temperature (but nondegenerate) plasma regime, and is manifest in the ion-ion distributions $g_n(R)$ computed, for example, by Dharma-Wardana and Perrot[26] using finite-temperature density-functional theory, and by Tanaka and Ichimaru[27] using the hypernetted-chain scheme. There are no simple formulas or prescriptions that reproduce these cited results, but it is well known that—for plasma conditions of interest here—the $V_n(R)$ values from both of these theoretical approaches are well approximated (except for $R\approx 0$) by Monte Carlo simulations, for which accurate fitting formulas do exist (see, e.g., Itoh *et al.*, Ref. 28). As Fig. 10 shows, our simple expression, Eq. (6), agrees very well with the fits to Monte Carlo data. In the vicinity of $R=0$, where Monte Carlo data do not exist, the extent of screening indicated by our model, Eq. (6), is about midway between that predicted by the united-atom formula, Eq. (A7), and that predicted by the extrapolation of the (linear) fit to Monte Carlo data.

*Debye-Hückel model.* This calculation proceeds analogously. The electrostatic self-energy of electrons in a plasma having Debye radius $D$, due to polarization by a nucleus $Z_1$, is

$$V_{ee}^{(1)}=+\frac{1}{4}\frac{Z_1^2e^2}{D}, \tag{A9}$$

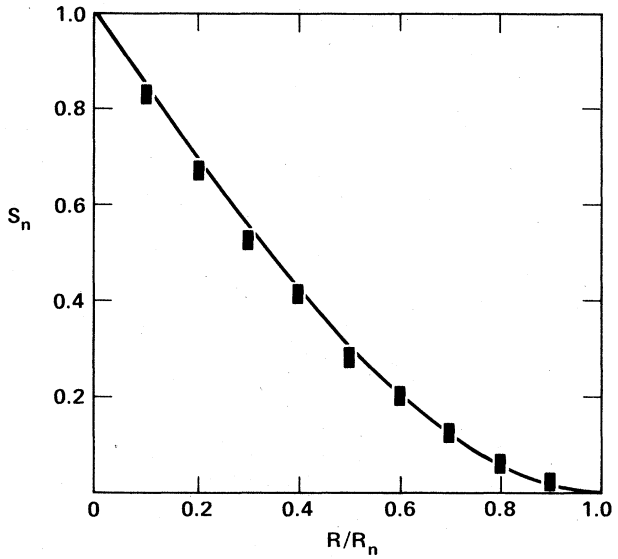


FIG. 10. The multiplicative factor $S_n=RV_n/Z_1Z_2e^2$ for screening in the ion-sphere model. The curve represents Eq. (6), while the filled rectangles represent fits to Monte Carlo (MC) data (Ref. 28), or—in the case of the inner two points—extrapolation of these fits to smaller values of $R/R_n$. The heights of the rectangles correspond to the variation of $S_n$ (MC) over the range of values of $Z_1/Z_2$ encountered in the present cross-section calculations (cf. Table III).

and the electrostatic interaction energy between this nucleus and all the plasma electrons is

$$V_{ez}^{(1)}=-\frac{Z_1^2e^2}{D}. \tag{A10}$$

Thus

$$V^{(1)}=V_{ee}^{(1)}+V_{ez}^{(1)}=-\frac{3}{4}\frac{Z_1^2e^2}{D} \tag{A11}$$

is the total electrostatic energy due to the screening of that one nucleus. (We assume that the other plasma ions are immobile, and form a charge-neutralizing background; hence, $D$ contains contributions from electrons only.)

Next, consider two nuclei $Z_1$ and $Z_2$, separated by a distance $R$, to be immersed in the plasma. Since the total electrostatic potential at a distance $\mathbf{r}$ from $Z_1$ is

$$\Phi(\mathbf{r})=\Phi_e(\mathbf{r})+\Phi_n(\mathbf{r})$$
$$=\frac{Z_1e}{r}\exp\left[-\frac{r}{D}\right]+\frac{Z_2e}{|\mathbf{R}-\mathbf{r}|}\exp\left[-\frac{|\mathbf{R}-\mathbf{r}|}{D}\right], \tag{A12}$$

where $\Phi_n$ is the unscreened nuclear contribution, it is straightforward to show that the electron charge density at $\mathbf{r}$ is

$$q_e(\mathbf{r})=-\frac{Z_1 e}{4\pi D^2 r}\exp\left[-\frac{r}{D}\right] -\frac{Z_2 e}{4\pi D^2|\mathbf{R}-\mathbf{r}|}\exp\left[-\frac{|\mathbf{R}-\mathbf{r}|}{D}\right] . \quad \text{(A13)}$$

With these expressions in hand, one can determine the total electrostatic energy of the two nuclei in the plasma,

$$V^{(12)}=\frac{Z_1 Z_2 e^2}{R}+\int d^3r\, q_e(\mathbf{r})[\tfrac{1}{2}\Phi_e(\mathbf{r})+\Phi_Z(r)] =\frac{Z_1 Z_2 e^2}{R}\left[1-\frac{R}{2D}\right]\exp\left[-\frac{R}{D}\right]-\frac{3e^2}{4D}(Z_1^2+Z_2^2) . \quad \text{(A14)}$$

When the energies $V^{(1)}$ and $V^{(2)}$ of the individual Debye-shielded nuclei are subtracted, one is left with the total interaction energy

$$V_n(R)=V^{(12)}-V^{(1)}-V^{(2)} =\frac{Z_1 Z_2 e^2}{R}\left[1-\frac{R}{2D}\right]\exp\left[-\frac{R}{D}\right] , \quad \text{(A15)}$$

which is presented in Eq. (7) in the main body of the paper. Again, we see that the interaction is weakly attractive at large values of $R$.

## APPENDIX B: MATRIX ELEMENTS AND SYMMETRIES

### 1. Matrix elements

Consider the matrix element of $1/|\mathbf{R}-\mathbf{r}|$,

$$W_{\alpha\alpha'}\equiv\left\langle\alpha\left|\frac{1}{|\mathbf{R}-\mathbf{r}|}\right|\alpha'\right\rangle . \quad \text{(B1)}$$

Substitution of the spherical harmonic expansion of $1/|\mathbf{R}-\mathbf{r}|$ into (B1) yields

$$W_{\alpha\alpha'}=\sum_{\lambda=0}^{\infty}\sum_{\mu=-\lambda}^{\lambda} Y^*_{\lambda\mu}(\theta',\phi')\langle\phi_\alpha|\,Y_{\lambda\mu}\,|\phi_{\alpha'}\rangle y_\lambda(nl,n'l') , \quad \text{(B2)}$$

where

$$\langle\phi_\alpha|\,Y_{\lambda\mu}\,|\phi_{\alpha'}\rangle=\int d\Omega\,\phi^*_{JlM_J}(\theta,\phi)\phi_{J'l'M'_J}(\theta,\phi)Y_{\lambda\mu}(\theta,\phi) , \quad \text{(B3)}$$

and

$$y_\lambda(nl,n'l')=\int_0^\infty r^2\frac{r_<^\lambda}{r_>^{\lambda+1}}\mathscr{R}_{nl}(r)\mathscr{R}_{n'l'}(r)dr . \quad \text{(B4)}$$

The $\mathscr{R}_{nl}$ are hydrogenic radial wave functions and the $\phi_{JlM_J}$ are coupled spin plus angular functions, that is,

$$|\phi_\alpha\rangle=|lSJM_J\rangle=(-1)^{S-l-M_J}\sum_{M_l=-l}^{l}\sum_{M_S=-S}^{S}(2J+1)^{1/2}\begin{bmatrix} l & S & J\\ M_l & M_S & -M_J\end{bmatrix}|lM_lSM_S\rangle . \quad \text{(B5)}$$

Thus, Eq. (B2) becomes

$$W_{\alpha\alpha'}=[(2J+1)(2J'+1)]^{1/2}(-1)^{S+S-l-l'-M_J-M'_J} \times\sum_{\lambda=0}^{\infty}\sum_{\mu=-\lambda}^{\lambda}\frac{4\pi}{2\lambda+1}Y^*_{\lambda\mu}(\theta',\phi')\sum_{M_l=-l}^{l}\sum_{M_S=-S}^{S}\sum_{M'_l=-l'}^{l'}\sum_{M'_S=-S}^{S}\langle lM_lSM_S\,|\,Y_{\lambda\mu}\,|\,l'M'_lSM'_S\rangle \times\begin{bmatrix} l & S & J\\ M_l & M_S & -M_J\end{bmatrix}\begin{bmatrix} l' & S & J'\\ M'_l & M'_S & -M'_J\end{bmatrix}y_\lambda(nl,n'l') . \quad \text{(B6)}$$

The states $|lM_lSM_S\rangle$ are direct-product states $|lM_l\rangle\otimes|SM_S\rangle$, and so we have

$$\langle lM_lSM_S\,|\,Y_{\lambda\mu}\,|\,l'M'_lSM'_S\rangle=\langle lM_l\,|\,Y_{\lambda\mu}\,|\,l'M'_l\rangle\delta_{M_SM'_S} . \quad \text{(B7)}$$

Next, we use the relation

$$\langle lM_l\,|\,Y_{\lambda\mu}\,|\,l'M'_l\rangle=(-1)^{M_l}\left[\frac{(2l+1)(2l'+1)(2\lambda+1)}{4\pi}\right]^{1/2}\begin{bmatrix} l & \lambda & l'\\ -M_l & \mu & M'_l\end{bmatrix}\begin{bmatrix} l & \lambda & l'\\ 0 & 0 & 0\end{bmatrix} \quad \text{(B8)}$$

to reduce Eq. (B6) to

$$W_{\alpha\alpha'}=[4\pi(2J+1)(2J'+1)(2l+1)(2l'+1)]^{1/2}(-1)^{2S-l-l'-M_J-M'_J} \times\sum_{\lambda=0}^{\infty}\sum_{\mu=-\lambda}^{\lambda}\frac{Y^*_{\lambda\mu}(\theta',\phi')}{(2\lambda+1)^{1/2}}\begin{bmatrix} l & \lambda & l'\\ 0 & 0 & 0\end{bmatrix}y_\lambda(nl,n'l') \times\sum_{M_S=-S}^{S}\sum_{M_l=-l}^{l}(-1)^{M_l}\begin{bmatrix} l & S & J\\ M_l & M_S & -M_J\end{bmatrix}\sum_{M'_l=-l'}^{l'}\begin{bmatrix} l' & S & J'\\ M'_l & M_S & -M'_J\end{bmatrix}\begin{bmatrix} l & \lambda & l'\\ -M_l & \mu & M'_l\end{bmatrix} . \quad \text{(B9)}$$

Since $J$, $S$, $l$, and $M_J$ are all given, standard properties of the 3-$j$ symbols permit us to restrict the sum in Eq. (B9), which now becomes

$$W_{\alpha\alpha'}=(-1)^{2S-l-l'-M_J-M_J'}[4\pi(2J+1)(2J'+1)(2l+1)(2l'+1)]^{1/2}$$
$$\times\sum_{M_S=-S}^{S}(-1)^{M_l}\begin{bmatrix} l & S & J \\ M_l & M_S & -M_J\end{bmatrix}\begin{bmatrix} l' & S & J' \\ M_l' & M_S & -M_J'\end{bmatrix}$$
$$\times\sum_{\lambda=|l-l'|}^{l+l'}\frac{Y^*_{\lambda\mu}}{(2\lambda+1)^{1/2}}\begin{bmatrix} l & \lambda & l' \\ 0 & 0 & 0\end{bmatrix}\begin{bmatrix} l & \lambda & l' \\ -M_l & \mu' & M_l'\end{bmatrix}y_\lambda(nl,n'l')\ , \tag{B10}$$

where $M_l=M_J-M_S$, $M_l'=M_J'-M_S$, $\mu=M_l-M_l'=M_J-M_J'$.

### 2. Symmetry

Make explicit the dependence on $J$, $l$, $M_J$, etc., and consider the following matrix element:

$$W(J,l,-M_J;J',l',-M_J')$$
$$=(-1)^{2S-l-l'+M_J+M_J'}[4\pi(2J+1)(2J'+1)(2l+1)(2l'+1)]^{1/2}$$
$$\times\sum_{M_S=-S}^{S}(-1)^{-M_J-M_S}\begin{bmatrix} l & S & J \\ -M_J-M_S & M_S & M_J\end{bmatrix}\begin{bmatrix} l' & S & J' \\ -M_J'-M_S & M_S & M_J'\end{bmatrix}$$
$$\times\sum_{\lambda=|l-l'|}^{l+l'}\frac{Y^*_{\lambda,M_J'-M_J}}{(2\lambda+1)^{1/2}}\begin{bmatrix} l & \lambda & l' \\ 0 & 0 & 0\end{bmatrix}\begin{bmatrix} l & \lambda & l' \\ M_J+M_S & M_J'-M_J & -M_J'-M_S\end{bmatrix}y_\lambda(nl,n'l')\ . \tag{B11}$$

By using the property that

$$\begin{bmatrix} J_1 & J_2 & J_3 \\ m_1 & m_2 & m_3\end{bmatrix}=(-1)^{J_1+J_2+J_3}\begin{bmatrix} J_1 & J_2 & J_3 \\ -m_1 & -m_2 & -m_3\end{bmatrix} \tag{B12}$$

and by first defining $\tilde{M}_S=-M_S$, and reversing the resulting sum over $\tilde{M}_S$, Eq. (B11) becomes

$$W(J,l,-M_J',J',l',-M_J')$$
$$=(-1)^{2S-l-l'+M_J+M_J'}[4\pi(2J+1)(2J'+1)(2l+1)(2l'+1)]^{1/2}(-1)^{2S+l+l'+J+J'}$$
$$\times\sum_{\tilde{M}_S=-S}^{S}(-1)^{-M_J+\tilde{M}_S}\begin{bmatrix} l & S & J \\ M_J-\tilde{M}_S & -\tilde{M}_S & -M_J\end{bmatrix}\begin{bmatrix} l' & S & J' \\ M_J'-\tilde{M}_S & \tilde{M}_S & -M_J'\end{bmatrix}$$
$$\times\sum_{\lambda=|l-l'|}^{l+l'}\frac{Y^*_{\lambda,M_J'-M_J}}{(2\lambda+1)^{1/2}}\begin{bmatrix} l & \lambda & l' \\ 0 & 0 & 0\end{bmatrix}\begin{bmatrix} l & \lambda & l' \\ -M_J+\tilde{M}_S & M_J-M_J' & M_J'-\tilde{M}_S\end{bmatrix}y_\lambda(nl,n'l')\ . \tag{B13}$$

For $\phi'=0$ we have that $Y^*_{\lambda\mu}=(-1)^\mu Y_{\lambda-\mu}$. By using this a comparison of Eq. (B13) with Eq. (B10) yields

$$W(J,l,-M_J;J',l',-M_J')$$
$$=(-1)^{2(S+M_J+M_J')+M_J'-M_J+l+l'+J+J'}$$
$$\times W(J,l,M_J;J',l',M_J')\ . \tag{B14}$$

This reduces to

$$W(J,l,-M_J',J',l',-M_J')$$
$$=(-1)^{2S+l+l'+J+J'+M_J-M_J'}W(J,l,M_J;J',l,M_J')\ , \tag{B15}$$

since $2(M_J+M_J')$ is even. The second symmetry property that follows directly from Eq. (B10) can be obtained by considering $W_{\alpha'\alpha}$; it is obvious that

$$W_{\alpha'\alpha}=W_{\alpha\alpha'}\ . \tag{B16}$$

As a direct consequence of these two symmetry relations, it follows that

$$W(J,l,M_J;J,l-M_J)=-W(J,l,-M_J;J,l,M_J) \quad (S=\tfrac{1}{2}) \tag{B17}$$

and

$$W(J,l,M_J;J,l,-M_J)=+W(J,l,-M_J;J,l,M_J)\ , \tag{B18}$$

from which we get

$$W(J,l,M_J;J,l,-M_J)=0\ . \tag{B19}$$

A final result of symmetry (B15) is that

$$W(J,l,M_J;J,l,M_J)=W(J,l,-M_J;J,l,-M_J)\ . \tag{B20}$$

## APPENDIX C: THE RADIAL INTEGRALS

Consider the following integral:

$$y_\lambda(nl,n'l')\equiv\int_0^\infty r^2\frac{r_<^\lambda}{r_>^{\lambda+1}}\mathscr{R}_{nl}\mathscr{R}_{n'l'}\,dr\ , \tag{C1}$$

where $\mathscr{R}_{nl}$ is the (normalized) hydrogenic wave function, given by

$$\mathscr{R}_{nl}=-\left[\nu_n^3\frac{(n-l-1)!}{2n(n+l)!}\right]^{1/2}e^{-\nu_n r/2}(\nu_n r)^l L_{n-l-1}^{2l+1}(\nu_n r) \tag{C2}$$

with $\nu_n=2Z_A/n$ and $L_{n-l-1}^{2l+1}(\nu_n r)$ being the usual Laguerre polynomial.[29] In Eq. (C1), $r_<$ ($r_>$) is the smaller (larger) of $R$ (the distance between the nuclei) and $r$ (the magnitude of the bound-electron's position). Note that $\lambda$ is constrained to $0\le\lambda\le l+l'$. For transitions between fine-structure levels of the same manifold, $n=n'$. Substitution of Eq. (C2) into Eq. (C1) yields

$$y_\lambda(nl,nl')=\frac{\nu_n^3}{2n}\left[\frac{(n-l-1)!(n-l'-1)!}{(n+l)!(n+l')!}\right]^{1/2}\times\int_0^\infty e^{-\nu_n r}(\nu_n r)^{l+l'}L_{n-l-1}^{\Lambda}(\nu_n r)\times L_{n-l'-1}^{\Lambda'}(\nu_n r)r^2\frac{r_<^\lambda}{r_>^{\lambda+1}}dr\ , \tag{C3}$$

where $\Lambda=2l+1$, $\Lambda'=2l'+1$. By defining $\tilde{A}_{nll'}$ to be the coefficient of the integral and $x=\lambda_n r$, then Eq. (C3) becomes

$$y_\lambda(nl,nl')=\frac{\tilde{A}_{nll'}}{\nu_n^3}\int_0^\infty e^{-x}x^{l+l'+2}L_{n-l-1}^{\Lambda}(x)L_{n-l'-1}^{\Lambda'}(x)\frac{r_<^\lambda}{r_>^{\lambda+1}}dx$$
$$=A_{nll'}\nu_n\left[\frac{1}{\xi^{\lambda+1}}\int_0^\xi e^{-x}x^{l+l'+\lambda+2}L_{n-l-1}^{\Lambda}L_{n-l'-1}^{\Lambda'}dx+\xi^\lambda\int_\xi^\infty e^{-x}x^{l+l'+1-\lambda}L_{n-l-1}^{\Lambda}L_{n-l'-1}^{\Lambda'}dx\right], \tag{C4}$$

where $\xi=R\nu_n$ and $A_{nll'}=\tilde{A}_{nll'}/\nu_n^3$. Let $I_1$ be the first term in the large parentheses and $I_2$ the second term; we then have

$$y_\lambda(nl,nl')=A_{nll'}\nu_n(I_1+I_2)\ . \tag{C5}$$

Next, we expand the Laguerre polynomial[29]

$$L_s^\Lambda=\sum_{k=0}^{s}(-1)^k\begin{bmatrix}s+\Lambda\\ s-k\end{bmatrix}\frac{x^k}{k!}\ , \tag{C6}$$

so that

$$L_s^\Lambda L_p^{\Lambda'}=\sum_{k=1}^{s}\sum_{m=0}^{p}(-1)^{k+m}\begin{bmatrix}s+\Lambda\\ s-k\end{bmatrix}\begin{bmatrix}p+\Lambda'\\ p-m\end{bmatrix}\frac{x^{k+m}}{k!m!}\ . \tag{C7}$$

We have set $s=n-l-1$ and $p=n-l'-1$, and have taken $l'$ to be the smaller quantum number, so $p>s$. After some algebra Eq. (C7) reduces to

$$L_s^\Lambda L_p^{\Lambda'}=\sum_{k=0}^{s+p}D_{sp\Lambda\Lambda'}^k x^k\ , \tag{C8}$$

where

$$D_{sp\Lambda\Lambda'}^k=(-1)^k(p+\Lambda')!(s+\Lambda)!\sum_{i=k_{\min}}^{k_{\max}}\frac{1}{(k-i)!(\Lambda'+k-i)!(p-k+i)!(\Lambda+i)!(s-i)!i!} \tag{C9}$$

and where

$$k_{\min}=\max(0,k-p),\quad k_{\max}=\min(s,k)\ . \tag{C10}$$

The use of Eqs. (C8) and (C9) in the definitions of $I_1$ and $I_2$ eventually yields the final, simple result

$$I_1+I_2=\frac{1}{\xi^{\lambda+1}}\left[G_0-e^{-\xi}\sum_{t=0}^{2n+\lambda-1}G_t\xi^t\right], \tag{C11}$$

where

$$G_t=\sum_{r=r_{\min}}^{s+p}D_{sp\Lambda\Lambda'}^r F_{q+r}^{q-t+r}\ . \tag{C12}$$

The following definitions completely specify $G_t$:

$$r_{\min}=\max[0,t-(2+l+l'+\lambda)+1]\ , \tag{C13}$$

$$q=l+l'+\lambda+2\ , \tag{C14}$$

$$F_a^b = \begin{cases} \dfrac{a!}{(a-b)!} - \dfrac{j!}{(j-b)!}, & b \le j \\ \dfrac{a!}{(a-b)!}, & b > j \end{cases} \tag{C15}$$

with $j = a - 2\lambda - 1$. Altogether, Eqs. (C9)–(C15) define the radial integrals $y_l$.

*Examples.* Equation (C11) is trivial to program but its analytic form is not immediately transparent. We therefore present some examples of specific radial integrals. Within the $n=2$ manifold there are four nonvanishing cases: (a) $l=l'=0$, $\lambda=0$; (b) $l=1$, $l'=0$, $\lambda=1$; (c) $l=l'=1$, $\lambda=0$; (d) $l=l'=1$, $\lambda=2$.

*Case (a): $l=l'=\lambda=0$.* In this case, $q=2$, $s=1$, $p=1$, $\Lambda=1$, $\Lambda'=1$. Then,

$$G_t = \sum_{r=r_{\min}}^{2} D^r_{1111} F^{2-t+r}_{2+r} , \tag{C16}$$

where $r_{\min} = \max(0, t-1)$,

$$G_0 = \sum_{r=0}^{2} D^r_{1111} F^{2+r}_{2+r} . \tag{C17}$$

Note from Eq. (C16) that $F^m_m = m!$. The $D$'s are calculated from Eq. (C9),

$$D^0_{1111} = 4, \quad D^1_{1111} = -4, \quad D^2_{1111} = 1 . \tag{C18}$$

Thus $G_0 = 8$. Similarly, we find that $G_1 = 6$, $G_2 = 2$, $G_3 = 1$, and so

$$I_1 + I_2 = \frac{1}{\xi}[8 - e^{-\xi}(8 + 6\xi + 2\xi^2 + \xi^3)] , \tag{C19}$$

with $\xi = R\nu_n = 2Z_A R/n$ as defined previously. The other three cases can be worked out analogously, with the following results.

*Case (b): $l=\lambda=1$, $l'=0$;*

$$I_1 + I_2 = -\frac{3}{\xi^2}[24 - e^{-\xi}(24 + 24\xi + 12\xi^2 + 4\xi^3 + \xi^4)] . \tag{C20}$$

*Case (c): $l=l'=1$, $\lambda=0$;*

$$I_1 + I_2 = \frac{1}{\xi}[24 - e^{-\xi}(24 + 18\xi + 6\xi^2 + \xi^3)] . \tag{C21}$$

*Case (d): $l=l'=1$, $\lambda=2$;*

$$I_1 + I_2 = \frac{5}{\xi^3}[144 - e^{-\xi}(144 + 144\xi + 72\xi^2 + 24\xi^3 + 6\xi^4 + \xi^5)] . \tag{C22}$$

These expressions can easily be checked by directly carrying out the appropriate radial integrals.

*Permanent address: Physics Department, Rice University, Houston, TX 77251.


[1] C. Jordan, Astron. Astrophys. **34**, 69 (1974).

[2] For two examples of the many such calculations, see (a) M. J. Seaton, Mon. Not. R. Astron. Soc. **127**, 191 (1964); (b) A. Dalgarno, *Atoms in Astrophysics,* edited by P. G. Burke *et al.* (Plenum, New York, 1983), p. 103, and references therein.

[3] J. C. Stewart and K. D. Pyatt, Astrophys. J. **144**, 1203 (1966).

[4] A. Peres and A. Ron, Phys. Rev. A **13**, 417 (1976).

[5] V. A. Boiko, S. A. Pikuz, and A. Ya. Faenov, J. Phys. B **12**, 1889 (1979).

[6] J. Quant. Spectrosc. Radiat. Transfer **27**, 3 (1982). The entire issue is devoted to this subject.

[7] G. J. Hatton, N. F. Lane, and J. C. Weisheit, J. Phys. B **14**, 4879 (1981).

[8] J. Davis and M. Blaha, in *Physics of Electronic and Atomic Collisions,* edited by S. Datz (North-Holland, Amsterdam, 1982), p. 811.

[9] B. L. Whitten, N. F. Lane, and J. C. Weisheit, Phys. Rev. A **29**, 945 (1984); *ibid.* **30**, 650 (1984).

[10] R. S. Pundir and K. C. Mathur, J. Phys. B **17**, 4245 (1984).

[11] M. J. Seaton, Proc. Phys. Soc. London **68**, 457 (1955).

[12] G. W. Erickson, J. Phys. Chem. Ref. Data **6**, 831 (1977).

[13] J. C. Weisheit, in *Applied Atomic Collision Physics,* edited by H. S. W. Massey (Academic, New York, 1984), Vol. II.

[14] R. W. Chappell, J. Cooper, and E. W. Smith, J. Quant. Spectrosc. Radiat. Transfer **9**, 149 (1969).

[15] B. F. Rozsnyai, J. Quant. Spectrosc. Radiat. Transfer **22**, 337 (1979).

[16] A. V. Vinogradov and V. P. Shevelko, Zh. Eksp. Teor. Fiz. **71**, 1037 (1976) [Sov. Phys.—JETP **44**, 542 (1976)].

[17] E. L. Pollock and J. C. Weisheit, in *Spectral Line Shapes* (de Gruyter, Berlin, 1985), Vol. 3.

[18] V. M. Burke and R. McCarroll, Proc. Phys. Soc. London **80**, 422 (1962).

[19] A. Burgess, D. G. Hummer, and J. A. Tully, Philos. Trans. R. Soc. London, Ser. A **266**, 225 (1969).

[20] M. Rotenberg, R. Bivins, N. Metropolis, and J. K. Wooten, Jr., *The 3-j and 6-j Symbols* (MIT Press, Cambridge, 1959).

[21] P. Faucher and D. A. Landman, Astron. Astrophys. **54**, 159 (1971); S. O. Kastner, *ibid.* **54**, 255 (1977); O. Bely and P. Faucher, *ibid.* **6**, 88 (1970); D. A. Landman, Sol. Phys. **31**, 81 (1973).

[22] J. M. Blatt and V. E. Weisskopf, *Theoretical Nuclear Physics* (Springer-Verlag, Berlin, 1952).

[23] R. Walling and J. C. Weisheit (unpublished).

[24] S. Ichimaru, Rev. Mod. Phys. **54**, 1017 (1982).

[25] E. E. Salpeter, Aust. J. Phys. **7**, 373 (1954).

[26] M. C. W. Dharma-wardana and F. Perrot, Phys. Rev. A **26**, 2096 (1982).

[27] S. Tanaka and S. Ichimaru, J. Phys. Soc. Jpn. **53**, 2039 (1984).

[28] N. Itoh, H. Totsuji, S. Ichimaru, and H. E. DeWitt, Astrophys. J. **234**, 1079 (1979).

[29] *Handbook of Mathematical Functions,* Natl. Bur. Stand. (U.S.), Appl. Math. Ser. No. 55, edited by M. Abramowitz and I. Stegun (U.S. GPO, Washington, D.C., 1964).